ACS SENSORS

pubs.acs.org/acssensors

Article

Poly(acrylic acid) Hydrogel Microspheres for a Metal-Ion Sensor

Hao Tan and Soo-Young Park*

Cite This: *ACS Sens.* 2021, 6, 1039−1048

Read Online

ACCESS | Metrics & More | Article Recommendations | Supporting Information

ABSTRACT: Monodispersed cross-linked poly(acrylic acid) (PAA) droplets (PAA X-droplets), prepared using the microfluidic method with in situ ultraviolet curing, were used as small spherical sensors to simultaneously detect both Ca^{2+} and Mg^{2+} in human saliva and serum. The PAA X-droplet treated with KOH (PAA_{KOH} X-droplet) was used as a reference droplet because of its highly swollen state. The PAA_{KOH} X-droplets shrunk in response to the presence of divalent metal ions (Ms) by forming a bridged structure of COO−M−OOC. The sizes of the PAA_{KOH} X-droplets were precisely and dynamically monitored in the poly(dimethylsiloxane) (PDMS) channel with passing time when the aqueous metal-ion solutions were flowing at a controlled flow rate. The sizes of the PAA_{KOH} X-droplets continuously decreased to the saturated constant size. The saturated size of the PAA_{KOH} X-droplet did not change; however, the speed of size reduction increased with an increase in the concentration of the divalent metal ion. The saturated size was studied using the saturated diameter ratio ($R_{sat\text{-}dia}$) with respect to the initial diameter of the PAA_{KOH} X-droplet before the metal-ion treatment, and the speed of the size reduction was investigated using the inverse time to reach half the saturated diameter reduction ($T_{1/2}{}^{-1}$). Ca^{2+} and Mg^{2+} exhibited $R_{sat\text{-}dia}$ values of 75.9 and 83.6%, respectively, when the flow rate was 5 μL min^{-1}, regardless of the metal concentration. The $T_{1/2}{}^{-1}$s for the Ca^{2+} and Mg^{2+} linearly increased with an increase in their concentrations. The $R_{sat\text{-}dia}$ of the aqueous Ca^{2+}/Mg^{2+} mixture solution had a linear relationship with φ [= $C_{Ca}/(C_{Ca} + C_{Mg})$, where C_{Ca} and C_{Mg} are the molar concentrations of Ca^{2+} and Mg^{2+}, respectively]. The $T_{1/2}{}^{-1}$ of the aqueous Ca^{2+}, Mg^{2+} mixture solution was calculated by adding the individual $T_{1/2}{}^{-1}$s of pure aqueous Ca^{2+} and Mg^{2+} solutions. Using the $R_{sat\text{-}dia}$ and $T_{1/2}{}^{-1}$ of the Ca^{2+}/Mg^{2+} mixture aqueous solution, the individual C_{Ca} and C_{Mg} in the mixture solution were successfully calculated. This method was applied to the human saliva and serum in which the major metal ions are Ca^{2+} and Mg^{2+}, and other metal ions existed in undetectable amounts by the PAA_{KOH} X-droplets. This method is simple, cost-effective, and highly accurate and solves the hurdles of separating the interference effect of a Mg^{2+} ion when a Ca^{2+} ion is measured in biofluids.

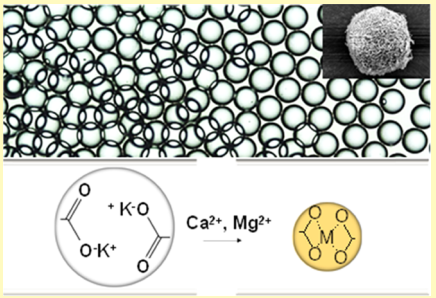

KEYWORDS: *calcium, biosensor, hydrogel, microfluidics, poly(acrylic acid), magnesium*

Calcium is one of the most abundant minerals in the human body. Most (~99%) of it is stored in bones and teeth. Only a small amount of calcium exists in blood and biofluids. In addition to strengthening bones and teeth, calcium is essential in some biological functions such as muscle contraction, blood vessel control, neurotransmitter release, hormone secretion, and blood clotting.[1,2] A convenient noninvasive calcium test can be used to detect diseases such as damaged bones, heart, nerves, kidneys, and other organs, and reduce the burden of the daily collection of blood samples. In the human body, calcium exists in bound and unbound ionized forms. Only the level of unbound Ca^{2+} matters for a body's function.[3,4] The normal levels of total calcium for a healthy human are 2.2−2.7 mM in serum[5] and approximately 2 mM in saliva.[6] Various probes have been employed for sensing calcium ions in the past few decades. These probes include organic dyes,[7,8] proteins,[9,10] magnetic nanoparticles,[11] and gold nanoparticles.[12] In modern biomedical science, fluorescent probes are helpful for the quantitative detection of Ca^{2+} owing to their high sensitivity and accuracy.[13−17] However, most fluorescent probes depend on organic molecules or fluorescent nanoparticles, which are poisonous to the biosystem.[18] Colorimetric methods also attract considerable attention owing to the convenient detection of Ca^{2+} without the necessity for a spectrophotometer.[19,20] For example, photonic interpenetrating polymer network (IPN) sensor array films,[21] in which a cross-linked PAA intertwines with a networked cholesteric liquid crystal, demonstrate the successful detection of Ca^{2+} in human saliva and serum. When sensing Ca^{2+}, the wavelength at the photonic band gap of an IPN film is inversely proportional to the Ca^{2+} concentration. This allows the amount of Ca^{2+} to be measured from the reflected light with naked eyes. However, this method suffers from interference from Mg^{2+} because the main metal ions in human serum are Ca^{2+} and Mg^{2+}, and other metal ions exist in

Received: October 29, 2020
Accepted: January 6, 2021
Published: January 18, 2021

https://dx.doi.org/10.1021/acssensors.0c02269
ACS Sens. 2021, 6, 1039−1048

an undetectably small amount.[22] Thus, methods to exclude (or measure simultaneously) Mg^{2+} during the measurement of Ca^{2+} are in high demand. Rasouli et al.[23] have reported a chromogenic reagent method for the simultaneous determination of Ca^{2+} and Mg^{2+} based on their complexation formations with 1-(1-hydroxy-4-methyl-2-phenylazo)-2-naphthol-4-sulfonic acid. By the technique of radial basis function−partial least squares to analyze the data of the ultraviolet−visible (UV−vis) spectra, the concentrations of Ca^{2+} and Mg^{2+} were successfully measured in various vegetable samples by the multivariate curve resolution with alternating least squares and rank annihilation factor analysis methods. However, the expensive one-time-use test reagent and complicated data treatment limit its wide application. Instead, the volumetric change of hydrogel can be used as a convenient tool for sensors because hydrogels can be considerably swollen by external stimuli. The cross-linked polyelectrolytes are charged hydrogels, which can be classified as anionic/cationic and weak/strong depending on the charge state and pH dependency, respectively. Poly(acrylic acid) (PAA) is one of the weak polyelectrolyte hydrogels, and it can be applied to a smart sensor owing to the interactions between divalent (e.g., Ca^{2+}) ions and carboxylic groups.[24] Two carboxylic groups can produce a bridged structure mediated by a divalent Ca^{2+} so that the swelled poly(acrylic acid) (PAA) hydrogel can be shrunk by Ca^{2+}. The degree of shrinkage of the PAA hydrogel can be an indicator of the amount of Ca^{2+} in an aqueous solution.

In this study, a calcium sensor was fabricated using PAA hydrogel droplets located in a poly(dimethylsiloxane) (PDMS) chip. The PDMS chip was designed for flushing aqueous solutions in the droplet-storage chamber through the outlet. Uniformly sized PAA cross-linked droplets (X-droplets) with the same chemical composition[25] were produced by the microfluidic method with acrylic acid (AA) monomers and a cross-linker of *N*,*N*′-methylenebisacrylamide (MBA), by in situ UV polymerization. The fabricated X-droplets were functionalized with KOH in the PDMS chamber and used as an indicator of the concentration of calcium ions in an aqueous solution by continuous dynamic measuring of the X-droplets' size during the flow of an aqueous metal-ion solution at a constant flow rate. The speed of the size reduction and saturated size of the PAA_{KOH} X-droplets were successfully used to simultaneously measure both Ca^{2+} and Mg^{2+} in the human serum and saliva. Thus, these convenient and cost-effective PAA X-droplets in the PDMS chip can be applied to a calcium sensor, which can solve the interference problem from Mg^{2+} in human biofluids.

EXPERIMENTAL SECTION

Materials. Sodium dodecyl sulfate (SDS) (Daejung, South Korea), Pluronic F108 (BASF, Germany), mineral oil light (14.2−17.2 cSt, Sigma-Aldrich), ABIL EM 90 (Evonik Industries, Germany), Irgacure 500 (BASF, Germany), *N*,*N*′-methylenebisacrylamide (MBA) (Sigma-Aldrich), tripropyleneglycol diacrylate (TPGDA) (Sigma-Aldrich), octadecyltrichlorosilane (OTS) (Sigma-Aldrich), KOH (Duksan, South Korea), $CaCl_2$ (anhydrous, Yakuri pure chemicals, Japan), HNO_3 (Daejung, South Korea), human serum (P2918−20ML, Sigma-Aldrich), a calcium colorimetric assay kit (MAK022, Sigma-Aldrich), $Cu(NO_3)_2{\cdot}3H_2O$ (Junsei, Japan), $Zn(NO_3)_2{\cdot}6H_2O$ (Sigma-Aldrich), $Mg(NO_3)_2{\cdot}6H_2O$ (Sigma-Aldrich), $FeCl_2{\cdot}4H_2O$ (Samchun, South Korea), KCl (Duksan, South Korea), $NaNO_3$ (Duksan, South Korea), and $LiPO_4$ (Sigma-Aldrich) were used. AA (Daejung, South Korea) was filtered by activated alumina (~75 μm, Wako pure chemical industries, Japan) to remove the inhibitor [200 ppm (monomethyl ether hydroquinone, MEHQ)]. The saliva sample was donated by a healthy 31-year-old male. Deionized (DI) water obtained by a reverse-osmosis system (μPure RO, Romax, South Korea) was used for all experiments unless otherwise specified.

Setup of the Microcapillary Chip. A glass capillary with a co-flow/flow-focusing combined geometry was used to produce PAA droplets. Two tapered cylindrical glass capillary tubes [1b100-6, 1 mm outer diameter (OD), World precision instruments, Inc.] were inserted into a square glass tube [810−9917, 1.05 mm inner diameter (ID), 1.5 mm OD, Atlantic International Technologies] at both left and right sides. The OD of the round capillaries (1 mm) is comparable to the ID of the square capillary (1.05 mm); thus, a round capillary can be inserted into the square capillary to achieve tight-fitting and coaxial alignment. The round glass capillary was tapered using a micropipette puller (P-97, Sutter Instrument). Hydrophobic coating was performed with OTS as follows. The round capillary was washed using water, dried using air flow, and treated with oxygen plasma for 5 min using a plasma generator (FC-10005, Femto Science, South Korea). The treated capillary was inserted in a vial containing 2 wt % OTS in toluene for 60 min, dipped in pure toluene for another 20 min, sequentially washed with acetone, ethanol, and water, and finally dried using air flow. The microfluidic chip was fabricated on the slide glass. The height of the cylindrical glass tube on the slide glass was adjusted by a cover glass for the center of the cylindrical glass to be conveniently aligned at the center of the square glass tube. The two round tapered capillaries in the square capillary on the slide glass faced opposite directions, with the capillary having a smaller taper diameter on the left side as shown in Figure S1a. The left open end of the square capillary (inserted by the left-side round tapered capillary) was sealed using an epoxy glue with a plastic tip having a syringe needle, which was used for the inlet of the continuous phase. The right open end of the square capillary (inserted by the right-side round tapered capillary) was sealed using epoxy glue. The left-side round capillary and syringe tip on the slide glass were connected to a pneumatic microfluidic flow control system (MFCS-EZ, Fluigent, France) with a tigon tube to control the flow rate of the disperse and continuous phases, respectively.

Production of PAA Droplets. A mixture of AA, MBA, water, Irgacure 500, Pluronic F108, and SDS in different weight ratios was used in the disperse phase; Irgacure 500 (6 wt %), Pluronic F108 (1.5 wt %), and SDS (0.25 wt %) were used at the fixed ratio, and the amount of other components was controlled. Mineral oil containing ABIL EM90 (3 wt %) was used for the continuous phase. The aqueous droplets were subsequently polymerized downstream in the collection tube in a narrow area using ultraviolet (UV) light (Innocure 5000, Lichtzen, South Korea) focused using an optical lens as shown in Figure S1b. The PAA X-droplets in mineral oil were gathered in a 4 mL vial. The gathered PAA X-droplets were sequentially washed using toluene, acetone, ethanol, and water. The washed PAA X-droplets were stored in water and used for further tests.

pH and Metal-Ion Test of PAA_{KOH} Hydrogel Droplets in the PDMS Chip. The produced PAA X-droplets were tested in the chamber of the PDMS chips. The transfer of PAA X-droplets from the vial to the chamber was done using a tigon tube and a 3 mL syringe (ID = 0.97 mm). The PDMS chip was designed for testing the PAA X-droplets by flushing an aqueous solution in the droplet-storage chamber (length × width × height = 3500 × 290 × 80 μm^3) using a syringe pump (Legato 100, KD Scientific) as shown in Figure S1c. The flow rate (Q) in the PDMS chip was controlled at 5 μL min^{-1} in all experiments unless otherwise mentioned. The uniformly sized PAA X-droplets were tested in the chamber by flushing the corresponding 2−12 pH buffer solutions (0.25 mL). The size of the PAA X-droplets in the chamber was measured by Image J software. The PAA X-droplets were treated with KOH in the chamber of the PDMS chip by flowing an aqueous KOH solution (0.25 mL, 0.1 M) at Q = 5 μL min^{-1}. After the KOH treatment, the extra KOH solution was washed using water in the chip, and the KOH-treated PAA (PAA_{KOH}) X-

https://dx.doi.org/10.1021/acssensors.0c02269
ACS Sens. 2021, 6, 1039−1048

droplets were used for the detection of metal ions. The measured size of the PAA_{KOH} X-droplets in the chamber was averaged and used as an indicator of the concentration of metal ions in aqueous solutions. Aqueous Ca^{2+}, Mg^{2+}, Cu^{2+}, Zn^{2+}, Fe^{2+}, K^+, Na^+, and Li^+ solutions were prepared by dissolving $CaCl_2$, $Mg(NO_3)_2{\cdot}6H_2O$, $Cu(NO_3)_2{\cdot}3H_2O$, $Zn(NO_3)_2{\cdot}6H_2O$, $FeCl_2{\cdot}4H_2O$, KCl, $NaNO_3$, and $LiPO_4$ in water at designated concentrations. The metal-ion aqueous solution was flowed at Q = 5 μL min^{-1}. In the recycling tests, the Ca^{2+}-tested PAA_{KOH} ($PAA_{KOH\text{-}Ca}$) X-droplets were sequentially treated with HNO_3 (0.5 mL, 0.1 M), water (0.25 mL), and KOH (0.25 mL, 0.1 M) for the recycling test. The treatments using a pH buffer, KOH, and HNO_3 aqueous solutions were performed at Q = 50 μL min^{-1} for 5 min.

Measurements. The Ca^{2+} concentrations in human serum and saliva were detected using calcium colorimetric assay kits for comparison. We followed the recommended procedure to measure the concentration of free Ca^{2+} (C_{Ca}) in human serum and saliva. Briefly, 90 μL of the chromogenic reagent was added to each cuvette containing 50 μL of calcium standards or samples (human serum and saliva) and then mixed gently. Additionally, 60 μL of calcium assay buffers were added to the prepared mixture solutions in the cuvettes, mixed gently, and then reacted at room temperature for 5−10 min while being protected from light during the sample preparation and reaction. The UV absorbance of the samples at 575 nm was measured using a UV−vis spectrometer (UV-2401PC, Shimadzu, Japan). To make a standard curve (Figure. S2), calcium standard solutions with different known C_{Ca} values were prepared by adding 0, 2, 4, 6, 8, and 10 μL of standard solutions (5 mM) to each cuvette, adjusting the total volume to 50 μL with water. The human serum and saliva samples were prepared via ×4 dilution with water. The measured C_{Ca} values for the human serum and saliva samples were 2.60 and 1.34 mM, respectively, both of which were in the normal range.[5,26] The surface images of the PAA, PAA_{KOH}, and $PAA_{KOH\text{-}Ca}$ X-droplets were examined using a field emission scanning electron microscope (FESEM, SU8220, Hitachi, Japan) operating at an accelerating voltage of 15 kV. The samples for the scanning electron microscopy (SEM) analysis were freeze-dried using a freeze dryer (FD-1000, Rikakikai, Japan) and coated with platinum using an ion sputter coater (E-1030, Hitachi, Japan) at a voltage of 19−20 mA for 60 s. Optical microscopy images of the droplets were obtained using an optical microscope (Labophhot-pol, Nikon, Japan) with a digital camera (Infinity1, Teledyne Lumenera).

RESULTS AND DISCUSSION

Droplet Production. The produced PAA droplets without UV curing were unstable and could be agglomerated into large droplets immediately after emerging from the microfluidic channel. In situ UV curing was performed to obtain stable X-droplets to prevent this agglomeration. UV light was focused on a small spot on the collection tube of the microfluidic chip using an optical lens. When the disperse droplets were passed through this area, the drops became sticky and plugged the channel. To avoid the plugging of the channel by the droplets, the pressures of the disperse and continuous phases (P_d and P_c) must be sufficiently high (e.g., >40 mbar for P_c) for the droplets to quickly pass the UV-shed region; a pressure-control system is used in the microfluidic system. Thus, pressure represents the speed of the medium. However, when the velocity of the continuous phase is high, the shear stress becomes higher than the surface-tension force, which results in an increase in the capillary number (C_a) of the continuous phase and jetting in the microfluidic channel; the C_a of the continuous phase is defined by the equation $C_a = \eta u/\gamma$, where η, u, and γ are the viscosity, velocity of the continuous phase, and surface tension between the disperse and continuous phases, respectively.[27−29] To induce dripping in the microfluidic channel (i.e., low C_a), polar water was added to the disperse phase to increase γ. However, the produced droplets were agglomerated before reaching the in situ UV curing region in the channel, although spherical droplets were produced in the dripping mode. To solve this problem, surfactants were added to stabilize the droplet. Surfactants used in the disperse phase were Pluronic F108 (1.5 wt %) and SDS (0.25 wt %), and that in the continuous phases was ABIL EM90 (3 wt %). The droplet formation was tested under different conditions. The types of droplet formation are classified into widening jetting, narrowing jetting, dripping, and failure (conditions when droplets are not produced); their typical photographic images are shown in Figure 1a. The droplets were produced under several conditions such as without water and surfactants (mode I), with 20 wt % water in the disperse phase and without surfactants (mode II), and with 20 wt % water in the disperse phase and surfactants (mode III). Figure 1b-i shows the droplet formation matrix at different

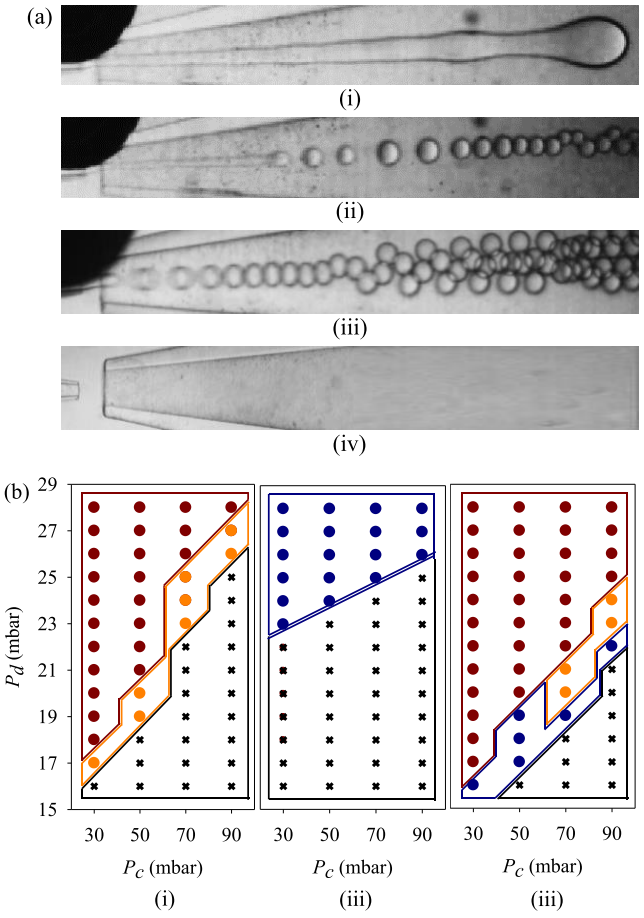

Figure 1. (a) Photographic images of the microfluidic chip during the production of droplets under (i) widening jetting, (ii) narrowing jetting, (iii) dripping, and (iv) failure modes; the disperse phase is an AA mixture containing AA (70.5 wt %, monomer), MBA (3.0 wt %, cross-linker), Irgacure 500 (6 wt % initiator), Pluronic F108 (1.5 wt %, surfactant), SDS (0.25 wt %, surfactant), and water (20 wt %); the continuous phase is a mineral oil mixed with EM 90 (3 wt %, surfactant). (b) Type of droplet formation at different P_d and P_c (i) without water and surfactants (mode I), (ii) with 20 wt % water in the disperse phase and without surfactants (mode II), and (iii) with 20 wt % water in the disperse phase and surfactants (mode III); red, orange, and blue dots and the × symbol represent widening jetting, narrowing jetting, dripping, and failure modes, respectively.

https://dx.doi.org/10.1021/acssensors.0c02269
ACS Sens. 2021, 6, 1039−1048

P_d and P_c without water and surfactants (mode I). When P_d decreases at a fixed P_c, the droplet formation changes from widening jetting to narrowing jetting and then to failure. The droplets with dripping mode could not be produced in mode I. Figure 1b-ii shows the droplet formation matrix at different P_d and P_c with 20 wt % water and without surfactants (mode II). The droplets were produced under dripping mode at all studied P_d and P_c because of the high interfacial energy between disperse and continuous phases (i.e., decreased C_a), as mentioned before. However, the produced droplets were agglomerated before reaching the in situ UV curing region in the channel. Figure 1b(iii) shows the droplet formation matrix at different P_d and P_c with water and surfactants (mode III). When P_d decreases at fixed P_c, the droplets are produced under widening jetting to narrowing jetting and to dripping modes. The droplets produced under dripping modes could be produced with a narrow window of P_d and P_c. Thus, uniform and stable droplets could be produced in mode III by adding water and surfactants and in situ curing in the microfluidic channel. The droplets produced at P_d = 18 mbar and P_c = 50 mbar were used for further experiments unless otherwise mentioned.

Figure 2a,b shows the photographic images of the produced droplets without (before) and with in situ UV curing,

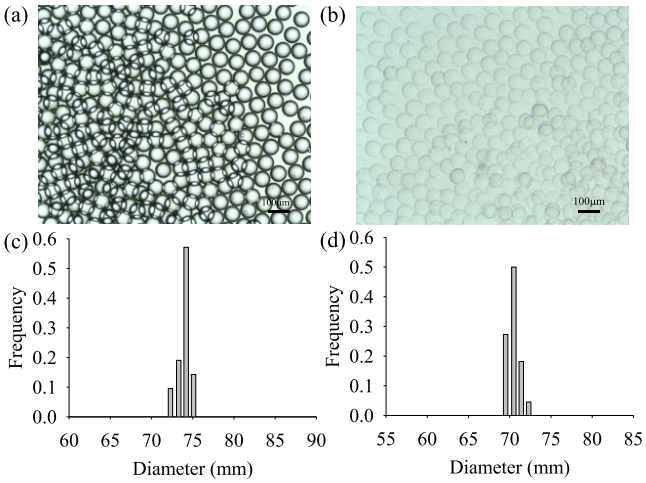

Figure 2. (a, b) Optical microscope images and (c, d) diameter size distributions of the PAA X-droplets in mineral oil (a, c) without and (b, d) with in situ UV curing.

respectively. The diameter of the droplet decreases from 73.4 ± 1.1 μm (Figure 2c) to 70.0 ± 1.2 μm (Figure 2d) when the droplets are formed by UV curing owing to a more dense structure that is formed by cross-linking. Small standard deviations indicate that the size of the droplet is uniform. The diameter of the X-droplets increased from 70.0 to 88.2 μm after the mineral oil medium was replaced with water for further water-based experiments. This increase is due to the hydrophilic nature of PAA.[30]

Stability of the X-Droplet. The stability of the X-droplet in an alkali solution was tested with different types of cross-linkers such as TPGDA and MBA, which carry ester and amide linkages, respectively. The stability in the alkali solution was tested because the PAA X-droplet was treated with a KOH solution to maximize the X-droplet size by blocking hydrogen bonds between carboxylic groups through the complex formation of COO^-K^+ (vide infra). Figure S3a,b shows the optical microscope images of the produced X-droplets cross-linked with TPGDA (0.95 mol %) and MBA (0.95 mol %), respectively, with different passing times (t_{pass}s) in an aqueous KOH solution (1 M). The diameters of the X-droplets cross-linked with TPGDA (Figure S3a) are 131, 131, 139, 159, 210, and 259 μm at t_{pass} = 0 h (immediately), 0.5 h, 3 h, 6 h, 1 days, and 2 days, respectively, which indicates that the X-droplets cross-linked with TPGDA start to swell (be degraded) at t_{pass} = 3 h and are completely dismantled at t_{pass} = 4 days. However, the diameters of X-droplets cross-linked with MBA (Figure S3b) are constant at 113 μm at all tested t_{pass}s until 4 days, which indicates that the X-droplets cross-linked with MBA are quite stable in an alkali solution until 4 days; further experiments at longer t_{pass} have not been performed, although we believe that the X-droplets were stable at longer t_{pass}s. The weak stability of the X-droplets cross-linked with TPGDA is due to the easy hydrolysis of ester bonds in an alkali solution.[31,32] Thus, the X-droplets cross-linked with MBA were used for further experiments.

pH Responsivity of PAA X-Hydrogel Droplets. The pH response of the PAA X-droplets prepared at C_{MBA} = 1.5 and 3.0 wt % was tested in the PDMS chip. Figure S4 shows the diameter of the X-droplet as a function of pH. With an increase in pH, the diameters of X-droplets prepared at C_{MBA} = 1.5 and 3.0 wt % increase stepwise at pH = ∼5, which is similar to the pK_a of AA. However, the PAA X-droplets prepared at C_{MBA} = 1.5 wt % increase from 76 to 125 μm, and those at C_{MBA} = 3.0 wt % increase from 81 to 111 μm when pH crosses 5. The D_{shrink}/D_{swell}s (where D_{shrink} and D_{swell} are the diameters of the X-droplets at pH = 2 and 12, respectively) are 0.61 and 0.73 for the X-droplets prepared at C_{MBA} = 1.5 and 3.0 wt %, respectively. This difference occurs because the X-droplet with a higher cross-linking density causes less shrinking and swelling in response to pH change.

Surface Morphology of PAA and PAA_{KOH} X-Droplets. The porous structure of the X-droplets was studied with freeze-dried samples. Figure 3 shows the SEM images of the freeze-dried PAA, PAA_{KOH}, and $PAA_{KOH\text{-}Ca}$ X-droplets. All X-droplets exhibit porous structures that can be observed under low magnification [Figure 3(i)]. A more detailed internal structure can be observed from the SEM images with high magnification [Figure 3(ii)]. The SEM image of the PAA X-droplet (Figure 3a) shows a closed structure, while that of the PAA_{KOH} X-droplet (Figure 3b) exhibits a more open structure. This difference is due to the swollen structure of the PAA_{KOH} X-droplet by complex formation of COO^-K^+, which blocks hydrogen bonds between carboxylic groups, as mentioned before. The SEM image of the $PAA_{KOH\text{-}Ca}$ X-droplet (Figure 3c) shows the closed structure again with small spherical dots. The closed structure may be due to the formation of −COO−Ca−OOC− by the replacement of K^+ with Ca^{2+}.

PAA_{KOH} X-Droplet for Metal-Ion Detection. Ca^{2+} was detected with the PAA_{KOH} X-droplet in the PDMS chip as a model study. First, the PAA X-droplet was positioned in the middle of the channel of the PDMS chip by a syringe pump. The PAA X-droplet was treated with an aqueous KOH solution (0.1 mM) and then water at Q = 50 μL min^{-1} for 5 min to produce the PAA_{KOH} X-droplet in the channel. Figure 4a-i shows the optical microscopy image of the PAA_{KOH} X-droplet prepared at C_{MBA} = 3.0 wt %. When the aqueous $CaCl_2$ solution (10 mM) was flowed into the PDMS chip at Q = 5 μL min^{-1} for 10 min, the diameter of the PAA_{KOH} X-droplet (113 μm) shrank to 86 μm (Figure 4a-ii) due to the formation of

https://dx.doi.org/10.1021/acssensors.0c02269
ACS Sens. 2021, 6, 1039−1048

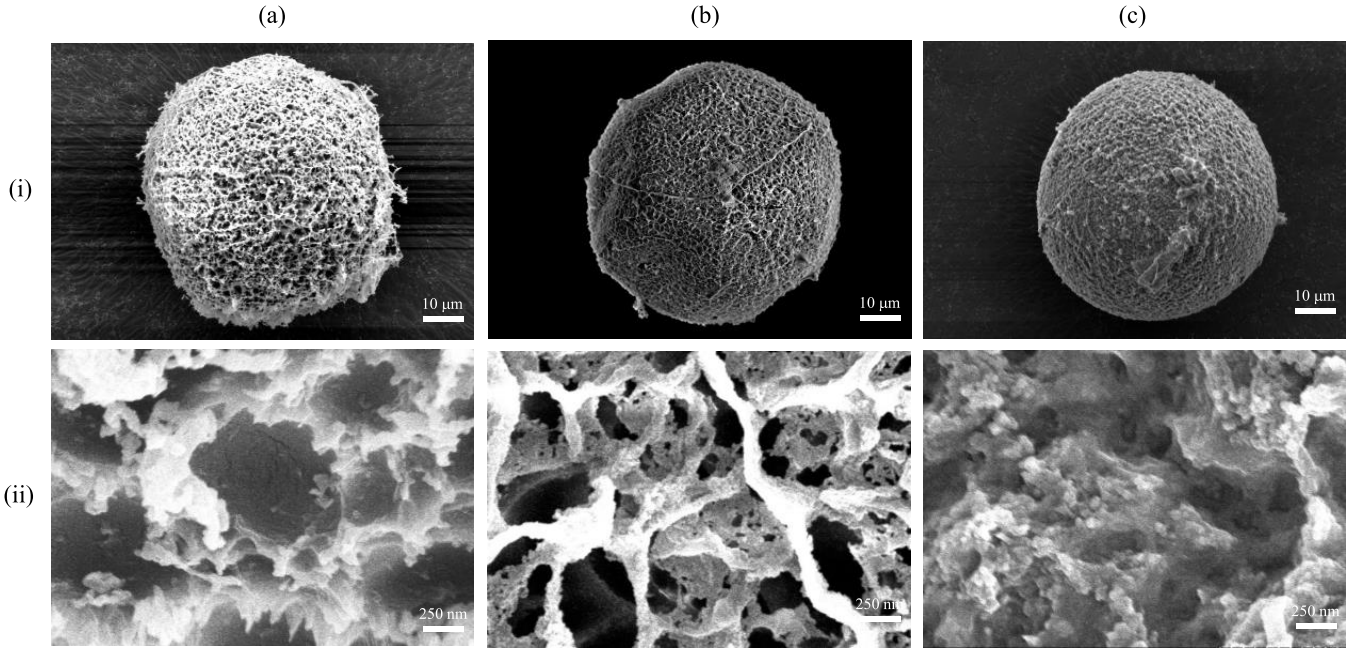

Figure 3. SEM images of (a) PAA, (b) PAA_{KOH}, and (c) PAA_{KOH-Ca} X-droplets at (i) low and (ii) high magnifications.

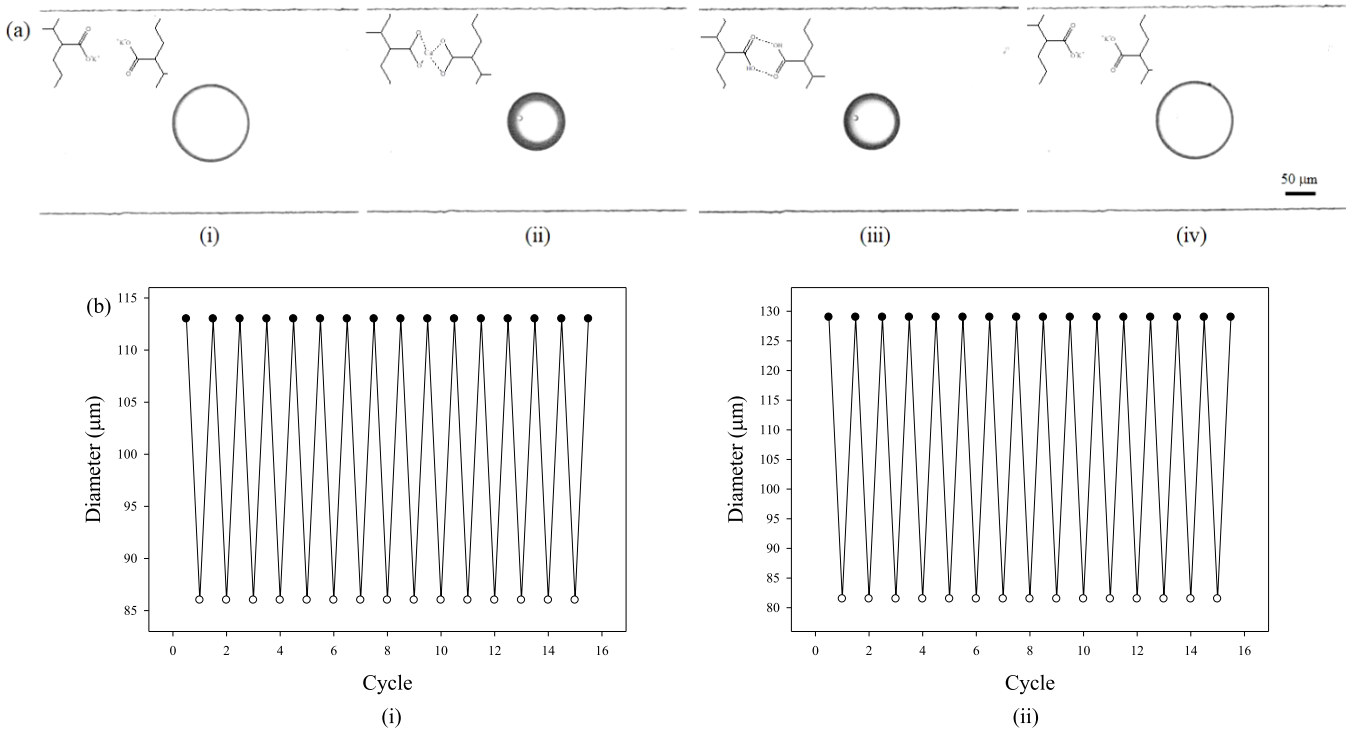

Figure 4. (a) Optical microscope images of (i) PAA_{KOH}, (ii) PAA_{KOH-Ca}, (iii) recovered PAA X-droplets after HNO_3 treatment, and (iv) recovered PAA_{KOH} in the PDMS chip; KOH (0.1 M), Ca^{2+} (10 mM), and HNO_3 (0.1 M) treatments were performed at Q = 50, 5, and 50 μL min^{-1} and t_{pass}, respectively. The chemical structure formation is shown in the inset figures. (b) Diameters of the recycled PAA_{KOH} (closed circle) and PAA_{KOH-Ca} (open circle) X-droplets prepared at C_{MBA} = (i) 3.0 wt % and (ii) 1.5 wt % as a function of recycling time. The scale bar in (a) is 50 μm.

COO−Ca−OOC bonds. The reusability (recycling) test was performed after HNO_3 and KOH treatments. When the PAA_{KOH-Ca} X-droplet was treated with HNO_3 by flowing an aqueous HNO_3 solution (0.1 mM) at Q = 50 μL min^{-1} for 10 min, the diameter of the PAA_{KOH-Ca} X-droplet (86 μm) decreased to 77 μm (Figure 4a-iii). The diameter did not considerably change with the HNO_3 treatment compared to that obtained with KOH and Ca^{2+} treatments. This occurs because the recovered −COOH groups can establish hydrogen bonds and prevent swelling by water. The recovered PAA X-droplets were treated with a KOH aqueous solution (0.1 mM) and water again at Q = 50 μL min^{-1} for 5 min to prepare the recovered PAA_{KOH} X-droplets. The recovered PAA_{KOH} X-droplet had a diameter of 113 μm (Figure 4a-iv), which was

https://dx.doi.org/10.1021/acssensors.0c02269
ACS Sens. 2021, 6, 1039−1048

the same as that of the original PAA_{KOH} X-droplets (113 μm). These recovered PAA_{KOH} X-droplets were further tested with the same $CaCl_2$ solution. This process was performed for several cycles to test the reusability of the PAA_{KOH} X-droplet for metal-ion detection. Figure 4b-i,ii shows the diameters of the PAA_{KOH} (after HNO_3 and KOH treatments) and $PAA_{KOH\text{-}Ca}$ (after Ca^{2+} test) X-droplets prepared at C_{MBA} = 3.0 and 1.5 wt %, respectively, as a function of recycling time. The diameters of PAA_{KOH} and $PAA_{KOH\text{-}Ca}$ X-droplets prepared at C_{MBA} = 3.0 wt % are nearly constant at 113 and 86 μm, respectively, until 15 cycles (Figure 4b-i); we did not perform further cycle tests, although we believe that the diameter does not change with more cycles. Similar results were observed from PAA_{KOH} prepared at C_{MBA} = 1.5 wt %, except for the larger diameter of PAA_{KOH} and the smaller diameter of $PAA_{KOH\text{-}Ca}$ X-droplets (Figure 4b-ii). These results indicate that PAA_{KOH} X-droplets can be reused many times by the HNO_3 treatment.

Simultaneous Ca^{2+} and Mg^{2+} Detection. The simultaneous detection of both Ca^{2+} and Mg^{2+} was studied because Ca^{2+} and Mg^{2+} are the major metal-ion species in human serum and saliva, as mentioned before. First, the shrinkage behavior of the PAA_{KOH} X-droplet with aqueous Ca^{2+} solutions was studied. Figure 5a shows the R_{dia} of the PAA_{KOH} X-droplets (prepared at C_{MBA} = 3.0 wt %) as a function of t_{imm} with different concentrations of calcium (C_{Ca}) from 0.1 to 10 mM; R_{dia} is defined as the diameter ratio at t_{imm} with respect to the initial PAA_{KOH} X-droplet, and t_{imm} is defined as a period of time during the flowing of the aqueous Ca^{2+} solution. R_{dia} decreases slowly at the beginning, quickly after that, and then is saturated at the constant value. The R_{dia} vs t_{imm} curves at different C_{Ca} are similar to each other, except for the speed of decrease of R_{dia}; higher C_{Ca} results in a faster speed. It is surprising that saturated R_{dia}s ($R_{sat\text{-}dia}$s) are almost constant regardless of C_{Ca}, and only the speed of the decrease of R_{dia} is different with C_{Ca}. A longer time is required to shrink the X-droplet to the saturated state when an aqueous metal-ion solution with a low concentration is supplied to the PAA_{KOH} X-droplets at constant Q. For example, in Figure 5a, approximately 62 min is required for the PAA_{KOH} X-droplet to reach $R_{sat\text{-}dia}$ with a 0.1 mM Ca^{2+} aqueous solution, while 6.5 min is required for a 1 mM Ca^{2+} aqueous solution. The speed of decrease of R_{dia} can be defined as the inverse of t_{imm} to reach half the value of the decrease of $R_{sat\text{-}dia}$ $[(100 - R_{sat\text{-}dia})/2 \times 100\%]$ in the plot of R_{dia} vs t_{imm}. This half-time of t_{imm} is defined as $T_{1/2}$. For example, $T_{1/2}$ at C_{Ca} = 0.1 mM in Figure 5a is t_{imm} to reach R_{dia} of 88% $[100 - (100 - 76)/2 \times 100\%]$ and $T_{1/2}$ is 45.4 min (as shown by the dotted lines), which can be converted into ${T_{1/2}}^{-1}$ of 0.022 min^{-1}. The measured ${T_{1/2}}^{-1}$ as a function of C_{Ca} is shown in Figure 5c. A linear relationship is observed with a slope of 0.17 min^{-1} mM^{-1}. Figure S5 shows the R_{dia} of the PAA_{KOH} X-droplets prepared at C_{MBA} = 1.5 wt % as a function of t_{imm} with different C_{Ca} from 0.1 to 10 mM. Similarly, the PAA_{KOH} X-droplets prepared at C_{MBA} = 1.5 wt % show the same trend as the ones prepared at C_{MBA} = 3 wt % (i.e., constant $R_{sat\text{-}dia}$ regardless of C_{Ca} and different ${T_{1/2}}^{-1}$ with C_{Ca}), except for a different slope of 0.24 min^{-1} mM^{-1} in the plot of ${T_{1/2}}^{-1}$ vs C_{Ca}. This difference is due to the fast swelling of a less cross-linked droplet. The PAA_{KOH} X-droplets with C_{MBA} = 3 wt % were used for further experiments unless otherwise mentioned. The effect of Q of the analyte solution on the shrinkage rate of the PAA_{KOH} X-droplet was studied. Figure S6a shows the R_{dia} of PAA_{KOH} X-droplets as a function of t_{imm} when the aqueous $CaCl_2$ solutions (0.25 mM) were flowed at different Q. Similarly, $R_{sat\text{-}dia}$s are almost the same regardless of Q and only the speed of the decrease of R_{dia} increases when Q increases. Figure S6b shows the measured ${T_{1/2}}^{-1}$ from Figure S6a as a function of Q. ${T_{1/2}}^{-1}$ rapidly increases at Q < 15 μL min^{-1} and then slowly increases at 15 < Q < 30 μL min^{-1}. We could not perform experiments at Q > 30 μL min^{-1} owing to the machine limitation in the syringe pump. ${T_{1/2}}^{-1}$ increases when Q increases because a large quantity of Ca^{2+} is supplied when Q is high. The speed of

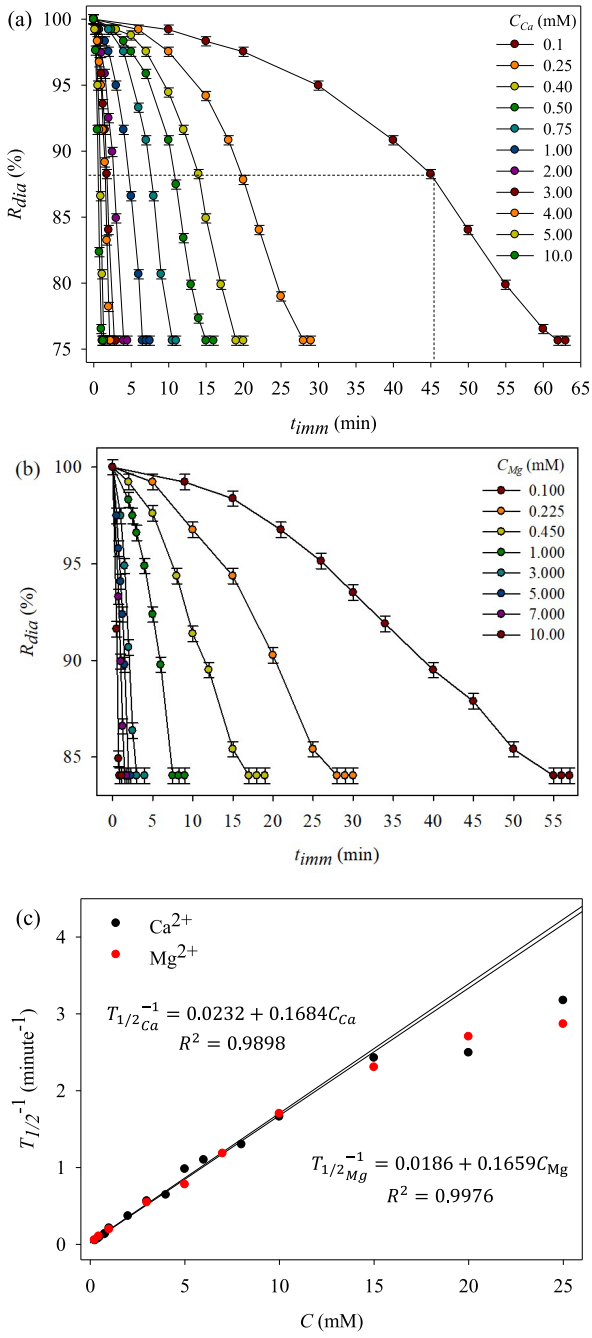

Figure 5. Diameter ratio (R_{dia}) of the PAA_{KOH} X-droplets prepared at C_{MBA} = 3.0 wt % as a function of t_{imm} at different (a) C_{Ca} and (b) C_{Mg} from 0.1 to 10 mM; t_{imm} is defined as the period of time during the flow of aqueous Ca^{2+} and Mg^{2+} solutions. (c) ${T_{1/2}}^{-1}$ in (a, b) as a function of C_{Ca} (or C_{Mg}); $T_{1/2}$ is the time required to reach half the value of the decrease in $R_{sat\text{-}dia}$ $[(100 - R_{sat\text{-}dia})/2 \times 100\%]$.

https://dx.doi.org/10.1021/acssensors.0c02269
ACS Sens. 2021, 6, 1039−1048

infiltration of Ca^{2+} ($T_{1/2}^{-1}$) should be saturated (constant) at a certain Q (it is not reached owing to machine limitation) when the diffusion of Ca^{2+} into the X-droplet is balanced with the outflow of Ca^{2+} from the X-droplet.

Next, the aqueous Mg^{2+} solution was tested because it exists in detectable amounts in human saliva and sweat, as mentioned before.[5,26] Figure 5b shows the R_{dia} of the PAA_{KOH} X-droplets (prepared at C_{MBA} = 3.0 wt %) as a function of t_{imm} at different Mg^{2+} concentrations (C_{Mg}) ranging from 0.1 to 10 mM during the flow of the aqueous Mg^{2+} solution. Again, $R_{sat\text{-}dia}$s was also the same regardless of C_{Mg} and only the speed of decrease of R_{dia} increases when C_{Mg} increases. The measured $T_{1/2}^{-1}$ as a function of C_{Mg} was drawn together with that of Ca^{2+} in Figure 5c. The slope of 0.17 min^{-1} mM^{-1} is the same as that of Ca^{2+} (0.17 min^{-1} mM^{-1}), which indicates that their binding abilities with carboxylic groups are similar; thus, both Ca^{2+} and Mg^{2+} should be considered together when human saliva and sweat are tested. The linear range and the limit of detection (LOD) were calculated with the equation

$$\mathrm{LOD} = 3.9 \times \left(\frac{\mathrm{SD}}{s}\right)$$

where SD is the standard deviation of the pseudo-blank sample and s is the corresponding slope of the graph in Figure 5. The blank sample was not available because KOH did not change in water so that the pseudo-blank sample (0.1 mM Ca^{2+} or Mg^{2+}) is employed.[33] The measured LOD/linear ranges of the Ca^{2+} and Mg^{2+} ions are 0.075/0.1−15 mM and 0.061/0.1−10 mM, respectively. Finally, the mixed Ca^{2+}/Mg^{2+} solutions with a different combination of C_{Ca} and C_{Mg} were tested. Figure 6a shows the R_{dia} of the PAA_{KOH} X-droplets (prepared at C_{MBA} = 3.0 wt %) as a function of t_{imm} during the flow of the mixed Ca^{2+}/Mg^{2+} aqueous solution with different (Ca^{2+}, Mg^{2+}) concentrations. $R_{sat\text{-}dia}$ and $T_{1/2}$ were measured from Figure 6a. When pure Ca^{2+} and Mg^{2+} aqueous solutions were tested, the $R_{sat\text{-}dia}$s were 75.9 and 83.6% for Ca^{2+} and Mg^{2+} aqueous solutions, respectively (Figure 5). If Ca^{2+} and Mg^{2+} independently contribute to $R_{sat\text{-}dia}$, then $R_{sat\text{-}dia}$ of the mixture solution is only dependent on the relative amount of Ca^{2+} (or Mg^{2+}), which can be defined as ϕ_{Ca} [= $C_{Ca}/(C_{Mg} + C_{Ca})$]. Figure 6b shows $R_{sat\text{-}dia}$ as a function of ϕ_{Ca}. There is a linear relationship between $R_{sat\text{-}dia}$ and ϕ_{Ca}. Thus, this result allows us to calculate ϕ_{Ca} (not individual C_{Ca} and C_{Mg}) from $R_{sat\text{-}dia}$. To investigate individual C_{Ca} (or C_{Mg}) from ϕ_{Ca}, the $T_{1/2}$ from the mixture solution was used. Because individual metal ion contributes independently to the diameter change (i.e., R_{dia}), $T_{1/2}^{-1}$ from the mixture solution can be added up by individual $T_{1/2}^{-1}$s from Ca^{2+} and Mg^{2+}, as shown in eq 1, where $T_{1/2Ca}^{-1}$ and $T_{1/2Mg}^{-1}$ are used from the equations shown in Figure 5c. Equation 1 can be converted into eq 2.

$$T_{1/2}^{-1} = T_{1/2_{Ca}}^{-1} + T_{1/2_{Mg}}^{-1} = 0.0418 + \left(\frac{1.2733}{83.6135 - R_{sat-dia}} + 0.0025\right)C_{Ca} \quad (1)$$

$$C_{Ca} = \frac{\left(\frac{1}{T_{1/2}} - 0.0418\right) \times (83.6135 - R_{sat-dia})}{1.4824 - 0.0025 \times R_{dia-sat}} \quad (2)$$

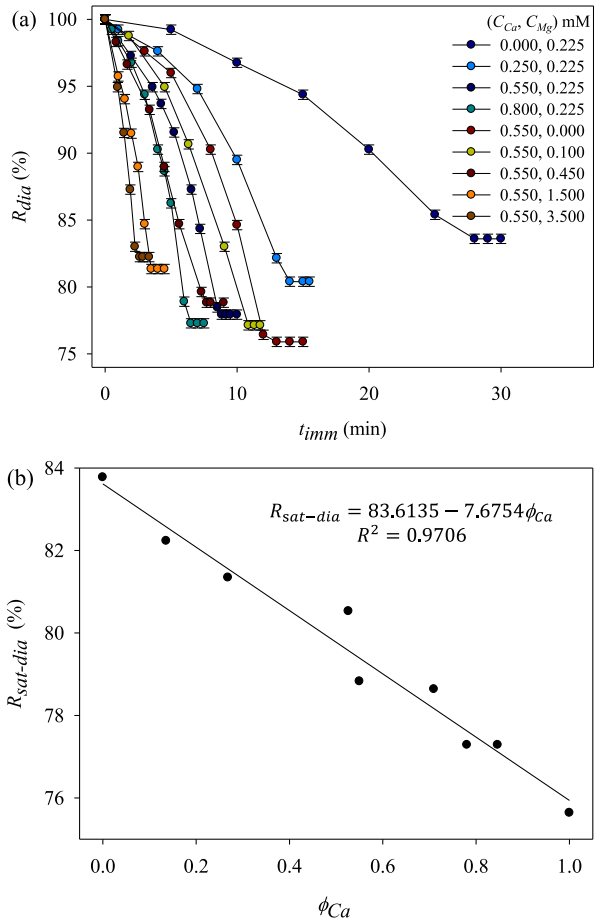

Figure 6. (a) R_{dia} of the PAA_{KOH} X-droplets (prepared at C_{MBA} = 3.0 wt %) as a function of t_{imm} during the flow of the aqueous Ca^{2+}/Mg^{2+} mixture solution with different (C_{Ca}, C_{Mg}) and (b) $R_{sat\text{-}dia}$ measured from (a) as a function of φ_{Ca} [= $C_{Ca}(C_{Mg} + C_{Ca})$].

C_{Ca} can be calculated by the $T_{1/2}^{-1}$ and $R_{sat\text{-}dia}$ measured from eq 2. Table 1 shows the comparison between the input and measured C_{Ca}s. The accuracy (defined by eq 3) of 82.2, 90.9, 99.5, 90.1, 89.2, 84.9, and 85.3% was obtained for mixture solutions with (C_{Ca}, C_{Mg} in mM) of (0.25, 0.225), (0.55, 0.100), (0.55, 0.225), (0.55, 0.450), (0.80, 0.225), (0.55, 1.500), and (0.55, 3.500), respectively.

$$\mathrm{Accuracy}\ (\%) = 100 - \left|\frac{\mathrm{Input}\ C_{Ca}(\mathrm{or}\ C_{Mg}) - \mathrm{Measured}\ C_{ca}(\mathrm{or}\ C_{Mg})}{\mathrm{Input}\ C_{Ca}}\right| \times 100 \quad (3)$$

High accuracy indicates that $R_{sat\text{-}dia}$ and $T_{1/2}^{-1}$ are good indicators for measuring the individual concentrations from the Ca^{2+}/Mg^{2+} mixture solution.

Other Metal-Ion Detection by PAA_{KOH} X-Droplets. Other metal ions, such as Fe^{2+}, Ca^{2+}, Cu^{2+}, Mg^{2}, K^{+}, Na^{+}, and Li^{+}, are tested with PAA_{KOH} X-droplets in the PDMS chip. Figure S7 shows the R_{dia} of the PAA_{KOH} X-droplet as a function of t_{imm}. The R_{dia}s of PAA_{KOH} X-droplets treated with K^{+}, Na^{+}, and Li^{+} (monovalent cations) are almost 100% until t_{imm} = 60 min because of the absence of coordinate covalent bond formation. The $R_{sat\text{-}dia}$s of Fe^{2+}, Ca^{2+}, Cu^{2+}, and Mg^{2+} are 74.6, 75.6, 76.6, and 84.0%, respectively. The $R_{sat\text{-}dia}$ of Mg^{2+} (84.0%) is bigger than those of the other three divalent cations, i.e., the PAA_{KOH} X-droplet is less shrunken. The $T_{1/2}^{-1}$s of Fe^{2+}, Ca^{2+}, Cu^{2+}, and Mg^{2+} are 0.21, 0.20, 0.21, and

https://dx.doi.org/10.1021/acssensors.0c02269
ACS Sens. 2021, 6, 1039−1048

Table 1. Input (C_{Ca}, C_{Mg}) and Measured (C_{Ca}, C_{Mg}) from the Aqueous Ca^{2+}/Mg^{2+} Mixture Solution

input (mM)					measured (mM)		accuracy[a] (%)	
Ca	Mg	$R_{sat\text{-}dia}$ (%)	$T_{1/2}$ (min)	ϕ_{Ca} (%)	Ca	Mg	Ca	Mg
0.25	0.225	80.4	8.07	52.6	0.21	0.29	82.2	73.1
0.55	0.100	77.1	7.08	84.6	0.50	0.09	90.9	92.4
0.55	0.225	77.9	6.03	71.0	0.55	0.19	99.5	85.6
0.55	0.450	78.8	4.90	55.0	0.60	0.36	90.1	81.0
0.80	0.225	77.3	4.50	78.0	0.89	0.19	89.2	83.5
0.55	1.500	81.3	2.51	26.8	0.63	1.51	84.9	99.5
0.55	3.500	82.2	1.60	13.6	0.69	3.13	85.3	82.2

[a]Equation 3.

Table 2. Comparison of Input C_{Ca} (from the Calcium Colorimetric Assay Kit) and Measured C_{Ca} (from $R_{sat\text{-}dia}$ and $T_{1/2}$) of the HypoCa, Normal, HyperCa1, and HyperCa2 Samples

		input (mM)			measured (mM)		
biofluid	sample	C_{Ca}	$R_{sat\text{-}dia}$ (%)	$T_{1/2}$ (min)	C_{Ca}	C_{Mg}	accuracy[a] (%)
serum	HyperCa1	2.60	78.1	1.63	2.45	0.94	94.4
	HyperCa2	1.15	76.8	4.25	1.02	0.13	88.8
	Normal	0.65	78.1	5.17	0.65	0.25	99.7
	HypoCa	0.32	78.1	9.15	0.29	0.11	90.8
saliva	HyperCa1	1.34	78.4	2.65	1.35	0.65	98.9
	HyperCa2	0.83	77.1	5.43	0.72	0.13	86.6
	Normal	0.33	78.4	8.85	0.29	0.14	86.9
	HypoCa	0.16	78.4	12.44	0.16	0.07	97.2

[a]Equation 3.

0.20 min^{-1}, respectively. The similar values of ${T_{1/2}}^{-1}$ indicate that the X-droplets are shrunk at a similar rate. The bigger value of $R_{sat\text{-}dia}$ for Mg^{2+} than other divalent cations may be due to the lower bridging strength between Mg^{2+} and $-COO^{-}$; Mg^{2+} is known to have a stable hydration shell, which decreases the absorption force of Mg^{2+} on $-COO^{-}$ compared to other divalent metal ions.[34]

Real Serum and Saliva Sample Test. Human serum and saliva samples were tested. Serum and saliva are viscous liquids that easily froth;[35] thus, human serum and saliva samples were diluted four times with water. For comparison with the real serum sample, artificial serum was prepared with a fourth (×0.25) concentration of the reported ones. The constituents of the prepared artificial serum are Na^{+} (34.85 mM), K^{+} (0.98 mM), Ca^{2+} (0.55 mM), Mg^{2+} (0.225 mM), Fe^{2+} (0.0045 mM), Cu^{2+} (0.0 0375 mM), and Zn^{2+} (0.00 325 mM); their concentrations are given in parentheses.[22] Figure S8 shows the R_{dia} of the PAA_{KOH} X-droplet as a function of t_{imm} for both the binary Ca^{2+}/Mg^{2+} (0.55, 0.225 mM) mixture and artificial serum samples; C_{Ca} and C_{Mg} are the same between the binary mixture and artificial serum samples. The curves of the Ca^{2+}/Mg^{2+} mixture and artificial solutions show small differences, which indicates that other metal ions with small amounts in the artificial serum sample do not affect the performance of Ca^{2+} and Mg^{2+} detection. Spike tests with real human serum and saliva were performed. The C_{Ca} values in the test samples are summarized in Table 2. The normal samples were prepared with the ×0.25 diluted samples so that C_{Ca}s for the ×0.25 diluted human serum and saliva are 0.65 and 0.33 mM, respectively. The HypoCa samples were prepared with the ×0.125 diluted sample so that the C_{Ca}s are 0.33 and 0.17 mM, respectively. The HyperCa1 samples were the original serum and saliva without dilution; thus, C_{Ca}s are 2.6 and 1.3 mM, respectively. The HyperCa2 samples are 0.5 mM higher than the normal samples; thus, C_{Ca}s are 1.15 and 0.83 mM, respectively. Figure 7a,b shows the R_{dia} of the PAA_{KOH} X-droplet as a function of t_{imm} during the flow of normal, HypoCa, HyperCa1, and HyperCa2 serum and saliva solutions, respectively. Surprisingly, the HypoCa, normal, and HyperCa2 serum samples show the same $R_{sat\text{-}dia}$ of 78.1% because φ_{Ca}s are the same for the three water-diluted samples. However, only $R_{sat\text{-}dia}$ of the HyperCa1 serum sample (extra Ca^{2+}-added sample) is 76.8%, which is lower than those of the other samples because φ_{Ca} is higher than those of the other diluted samples. Similarly, HypoCa, normal, and HyperCa2 saliva samples show the same $R_{sat\text{-}dia}$ of 78.4%, and the $R_{sat\text{-}dia}$ of the HyperCa1 sample (extra Ca^{2+}-added sample) is 77.1%, which is lower than those of the other samples. However, $T_{1/2}$s are different and strongly dependent on the metal-ion concentration. From $R_{sat\text{-}dia}$ and $T_{1/2}$, C_{Ca} can be calculated, as mentioned before. The test results are summarized in Table 2. The accuracies (defined by eq 3) are 94.4, 88.8, 99.7, and 90.8% for the HyperCa1, HyperCa2, normal, and HypoCa serum samples, respectively, and 98.9, 86.6, 86.9, and 97.2% for the HyperCa1, HyperCa2, normal, and HypoCa saliva samples, respectively. These results indicate that the PAA_{KOH} hydrogel can be used as a Ca^{2+} sensor with human blood and saliva samples.

CONCLUSIONS

The uniformly sized PAA_{KOH} X-droplets produced using a microfluidic method with in situ UV curing in the glass capillary chip can be used as a smart sensor to detect the presence of divalent ions in aqueous solutions. The saturated diameter ($R_{sat\text{-}dia}$) and speed of shrinkage (represented by ${T_{1/2}}^{-1}$) of the PAA_{KOH} X-droplet were precisely monitored in the narrow PDMS channel with t_{pass} during the flow of aqueous metal-ion solutions at a constant flow rate. $R_{sat\text{-}dia}$ was independent of the concentration of the divalent metal ion

https://dx.doi.org/10.1021/acssensors.0c02269
ACS Sens. 2021, 6, 1039−1048

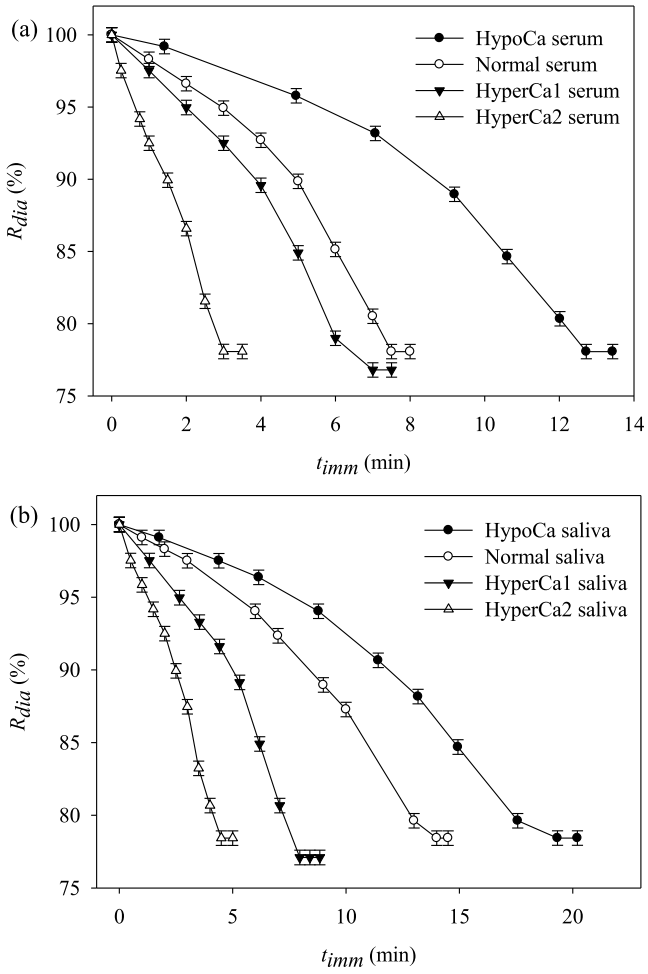

Figure 7. R_{dia} of the PAA_{KOH} X-droplet as a function of t_{imm} during the flow of normal, HypoCa, HyperCa1, and HyperCa2 (a) serum and (b) saliva solutions. Black circles, white circles, black triangles, and white triangles represent HypoCa, normal, HyperCa1, and HyperCa2 samples, respectively.

within our experimental range, but the $T_{1/2}^{-1}$ was strongly dependent on its concentration. Ca^{2+} and Mg^{2+} existing in human serum and saliva with detectable amounts were studied using the PAA_{KOH} X-droplet. The individual C_{Ca} and C_{Mg} in the aqueous Ca^{2+}/Mg^{2+} mixture solution can be separated from the analysis of both $R_{sat\text{-}dia}$ and $T_{1/2}^{-1}$. The PAA_{KOH} X-droplet was successfully applied to simultaneously measure both C_{Ca} and C_{Mg} in human serum and saliva. Thus, this new, simple, and innovative method is reusable, cost-effective, and highly accurate; it requires a small amount of sample and solves the issue of measuring both C_{Ca} and C_{Mg} with a single measurement by observing the size change of the hydrogel droplet in the designed PDMS chip.

■ ASSOCIATED CONTENT

Supporting Information

The Supporting Information is available free of charge at https://pubs.acs.org/doi/10.1021/acssensors.0c02269.

Experimental setups for microfluidic production of PAA_{KOH} X-droplets and the PDMS-based device for metal-ion sensing; standard plot of UV−vis absorbance at 575 nm vs C_{Ca} using calcium colorimetric assay kits; optical microscope images of the produced X-droplets cross-linked with TPGDA and MBA with different passing times in an aqueous KOH solution; diameter of PAA X-droplets as a function of pH; R_{dia} of PAA_{KOH} X-droplets (C_{MBA} = 1.5 wt %) as a function of t_{imm} at different C_{Ca}; R_{dia} vs t_{imm} of 0.25 mM aqueous $CaCl_2$ solutions flowed at different Q; R_{dia} vs t_{imm} of different metal solutions; aqueous Ca^{2+}/Mg^{2+} mixture solution and artificial serum samples flowed at 5 μL min^{-1}; and the measured $T_{1/2}^{-1}$ (PDF)

■ AUTHOR INFORMATION

Corresponding Author

Soo-Young Park − *School of Applied Chemical Engineering, Polymeric Nano Materials Laboratory, Kyungpook National University, Daegu 41566, Republic of Korea;* orcid.org/0000-0001-6796-4929; Email: psy@knu.ac.kr

Author

Hao Tan − *School of Applied Chemical Engineering, Polymeric Nano Materials Laboratory, Kyungpook National University, Daegu 41566, Republic of Korea*

Complete contact information is available at: https://pubs.acs.org/10.1021/acssensors.0c02269

Author Contributions

H.T. did all related experiments and wrote the manuscript, and S.-Y.P. supervised the work and revised the manuscript.

Notes

The authors declare no competing financial interest.

■ ACKNOWLEDGMENTS

This work was supported by the National Research Foundation of Korea (2020R1A2B5B02001556).

■ REFERENCES

(1) Beto, J. A. The role of calcium in human aging. *Clin. Nutr. Res.* **2015**, *4*, 1−8.

(2) Peacock, M. Calcium metabolism in health and disease. *Clin. J. Am. Soc. Nephrol.* **2010**, *5*, S23−S30.

(3) Kuo, I. Y.; Ehrlich, B. E. Signaling in Muscle Contraction. *Cold Spring Harbor Perspect. Biol.* **2015**, *7*, No. a006023.

(4) Ratz, P. H.; Murphy, R. A. Contributions of intracellular and extracellular Ca2+ pools to activation of myosin phosphorylation and stress in swine carotid media. *Circ. Res.* **1987**, *60*, 410−421.

(5) Goldstein, D. A. Serum Calcium. In *Clinical Methods: The History, Physical, and Laboratory Examinations*, 3rd ed.; Walker, H. K.; Hall, W. D.; Hurst, J. W., Eds.; Butterworths: Boston, 1990; Chapter 143.

(6) Kambalyal, P.; Kambalyal, P.; Hungund, S. Comparison of salivary calcium level in smokers and non-smokers with chronic periodontitis, aggressive periodontitis, and healthy controls. *J. Int. Soc. Prev. Community Dent.* **2015**, *5*, S68−S73.

(7) Johns, V. K.; Patel, P. K.; Hassett, S.; Calvo-Marzal, P.; Qin, Y.; Chumbimuni-Torres, K. Y. Visible light activated ion sensing using a photoacid polymer for calcium detection. *Anal. Chem.* **2014**, *86*, 6184−6187.

(8) Xie, X.; Zhai, J.; Crespo, G. A.; Bakker, E. Ionophore-based ion-selective optical nanosensors operating in exhaustive sensing mode. *Anal. Chem.* **2014**, *86*, 8770−8775.

(9) Yuan, H.; Xing, C.; An, H.; Niu, R.; Li, R.; Yan, W.; Zhan, Y. Ca2+-Controlled Assembly for Visualized Detection of Conformation Changes of Calmodulin. *ACS Appl. Mater. Interfaces* **2014**, *6*, 14790−14794.

(10) Wang, Y.; Tang, L.; Liu, W.; Zhao, Y.; Oscar, B. G.; Campbell, R. E.; Fang, C. Excited state structural events of a dual-emission

fluorescent protein biosensor for Ca^{2+} imaging studied by femtosecond stimulated Raman spectroscopy. *J. Phys. Chem. B* **2015**, *119*, 2204−2218.
(11) Taktak, S.; Weissleder, R.; Josephson, L. Electrode chemistry yields a nanoparticle-based NMR sensor for calcium. *Langmuir* **2008**, *24*, 7596−7598.
(12) Kim, S.; Kim, J.; Lee, N. H.; Jang, H. H.; Han, M. S. A colorimetric selective sensing probe for calcium ions with tunable dynamic ranges using cytidine triphosphate stabilized gold nanoparticles. *Chem. Commun.* **2011**, *47*, 10299−10301.
(13) Lin, Y.; Zheng, Y.; Guo, Y.; Yang, Y.; Li, H.; Fang, Y.; Wang, C. Peptide-functionalized carbon dots for sensitive and selective Ca^{2+} detection. *Sens. Actuators, B* **2018**, *273*, 1654−1659.
(14) Yue, J.; Li, L.; Cao, L.; Zan, M.; Yang, D.; Wang, Z.; Chang, Z.; Mei, Q.; Miao, P.; Dong, W.-F. Two-Step Hydrothermal Preparation of Carbon Dots for Calcium Ion Detection. *ACS Appl. Mater. Interfaces* **2019**, *11*, 44566−44572.
(15) Ankireddy, S. R.; Kim, J. Highly selective and sensitive detection of calcium (II) ions in human serum using novel fluorescent carbon dots. *Sens. Actuators, B* **2018**, *255*, 3425−3433.
(16) Kim, H. J.; Han, J. H.; Kim, M. K.; Lim, C. S.; Kim, H. M.; Cho, B. R. Dual-color imaging of sodium/calcium ion activities with two-photon fluorescent probes. *Angew. Chem.* **2010**, *122*, 6938−6941.
(17) Dong, X.; Han, J. H.; Heo, C. H.; Kim, H. M.; Liu, Z.; Cho, B. R. Dual-color imaging of magnesium/calcium ion activities with two-photon fluorescent probes. *Anal. Chem.* **2012**, *84*, 8110−8113.
(18) Lu, L.; An, X.; Huang, W. Quantitative determination of calcium ions by means of enhanced fluorescence of silver nanocluster complex. *Anal. Methods* **2017**, *9*, 23−27.
(19) Moirangthem, M.; Arts, R.; Merkx, M.; Schenning, A. P. An optical sensor based on a photonic polymer film to detect calcium in serum. *Adv. Funct. Mater.* **2016**, *26*, 1154−1160.
(20) Oh, J.; Eom, M. S.; Han, M. S. Co-functionalization with phosphate and carboxylate on polydiacetylene for colorimetric detection of calcium ions in serum. *Analyst* **2019**, *144*, 7064−7070.
(21) Myung, D.-b.; Hussain, S.; Park, S.-Y. J. S. Photonic calcium and humidity array sensor prepared with reactive cholesteric liquid crystal mesogens. *Sens. Actuators, B* **2019**, *298*, No. 126894.
(22) Ma, J.; Yan, L.; Guo, T.; Yang, S.; Liu, Y.; Xie, Q.; Ni, D.; Wang, J. Association between Serum essential Metal elements and the Risk of Schizophrenia in china. *Sci. Rep.* **2020**, *10*, No. 22463.
(23) Rasouli, Z.; Ghavami, R. Simultaneously detection of calcium and magnesium in various samples by calmagite and chemometrics data processing. *Spectrochim. Acta, Part A* **2016**, *169*, 72−81.
(24) Cannan, R. K.; Kibrick, A. Complex formation between carboxylic acids and divalent metal cations. *J. Am. Chem. Soc.* **1938**, *60*, 2314−2320.
(25) Kaminski, T.; Garstecki, P. Controlled droplet microfluidic systems for multistep chemical and biological assays. *Chem. Soc. Rev.* **2017**, *46*, 6210−6226.
(26) Teixeira, H. S.; Kaulfuss, S. M. O.; Ribeiro, J. S.; Pereira, B. D.; Brancher, J. A.; Camargo, E. S. Calcium, amylase, glucose, total protein concentrations, flow rate, pH and buffering capacity of saliva in patients undergoing orthodontic treatment with fixed appliances. *Dent. Press J. Orthod.* **2012**, *17*, 157−161.
(27) Utada, A. S.; Fernandez-Nieves, A.; Stone, H. A.; Weitz, D. A. Dripping to jetting transitions in coflowing liquid streams. *Phys. Rev. Lett.* **2007**, *99*, No. 094502.
(28) Utada, A. S.; Lorenceau, E.; Link, D. R.; Kaplan, P. D.; Stone, H. A.; Weitz, D. A. Monodisperse double emulsions generated from a microcapillary device. *Science* **2005**, *308*, 537−541.
(29) Lee, S. S.; Kim, B.; Kim, S. K.; Won, J. C.; Kim, Y. H.; Kim, S. H. Robust microfluidic encapsulation of cholesteric liquid crystals toward photonic ink capsules. *Adv. Mater.* **2015**, *27*, 627−633.
(30) Tanaka, T. Gels. *Sci. Am.* **1981**, *244*, 124−138.
(31) Browning, M. B.; Cosgriff-Hernandez, E. M. Development of a biostable replacement for PEGDA hydrogels. *Biomacromolecules* **2012**, *13*, 779−786.
(32) Browning, M.; Cereceres, S.; Luong, P.; Cosgriff-Hernandez, E. M. Determination of the in vivo degradation mechanism of PEGDA hydrogels. *J. Biomed. Mater. Res., Part A* **2014**, *102*, 4244−4251.
(33) Wenzl, T.; Haedrich, J.; Schaechtele, A.; Robouch, P.; Stroka, J. *Guidance Document on the Estimation of LOD and LOQ for Measurements in the Field of Contaminants in Feed and Food*; Publications Office of the European Union: Luxebourg, 2016.
(34) Rios-Carvajal, T.; Bovet, N.; Bechgaard, K.; Stipp, S.; Hassenkam, T. Effect of divalent cations on the interaction of carboxylate self-assembled monolayers. *Langmuir* **2019**, *35*, 16153−16163.
(35) Isho, B.; Abe, K. T.; Zuo, M.; Jamal, A. J.; Rathod, B.; Wang, J. H.; Li, Z.; Chao, G.; Rojas, O. L.; Bang, Y. M. Pu. a.; Christie-Holmes, N.; Gervais, C.; Ceccarelli, D.; Samavarchi-Tehrani, P.; Guvenc, F.; Budylowski, P.; Li, A.; Resources, A. P.; Yue, F. Y.; Marin, L. M.; Caldwell, L.; Wrana, J. L.; Colwill, K.; Sicheri, F.; Mubareka, S.; Gray-Owen, S. D.; Drews, S. J.; Siqueira, W. L.; Barrios-Rodiles, M.; Ostrowski, M.; Rini, J. M.; Durocher, Y.; McGeer, A. J.; Gommerman, J. L.; Gingras, A. C. Persistence of serum and saliva antibody responses to SARS-CoV-2 spike antigens in COVID-19 patients. *Sci. Immunol.* **2020**, *5*, No. eabe5511.

https://dx.doi.org/10.1021/acssensors.0c02269
ACS Sens. 2021, 6, 1039−1048